# A 79-GHz Radar Sensor in LTCC Technology Using Grid Array Antennas

Frank Bauer, *Student Member, IEEE*, Xin Wang, Wolfgang Menzel, *Fellow, IEEE*, and Andreas Stelzer, *Member, IEEE*

***Abstract*—Concept, design, and measurement results of a frequency-modulated continuous-wave radar sensor in low-temperature co-fired ceramics (LTCC) technology is presented in this paper. The sensor operates in the frequency band between 77–81 GHz. As a key component of the system, wideband microstrip grid array antennas with a broadside beam are presented and discussed. The combination with a highly integrated feeding network and a four-channel transceiver chip based on SiGe technology results in a very compact LTCC RF frontend (23 mm × 23 mm). To verify the feasibility of the concept, first radar measurement results are presented.**

***Index Terms*—Frequency modulated continuous wave (FMCW), laminated waveguide (LWG), low-temperature co-fired ceramic (LTCC), microstrip antenna arrays, millimeter-wave radar.**

## I. Introduction

DURING THE last years, millimeter-wave radar has seen a large increase in applications [1]. With respect to automotive radar, the frequency band between 77–81 GHz has been allocated for future medium-range radar (MRR) and short-range radar (SRR) applications, such as collision warning, blind spot detection, and pre-crash vehicle preparation [2], [3]. The rapid development of highly integrated multi-channel transceiver chips in SiGe technology [4], [5] enables the realization of compact and low-cost systems, which are a prerequisite for mass-market applications. A radar sensor based on low-temperature co-fired ceramics (LTCC) has, compared to traditional soft substrate materials, better mechanical stability and the advantage of higher thermal conductivity. Due to the high permittivity and excellent applicability for multi-layer designs, LTCC-based systems are perfectly suited for highly integrated designs. The high permittivity, however, also reduces the bandwidth and efficiency of radiating elements and makes the planar antenna design more challenging.

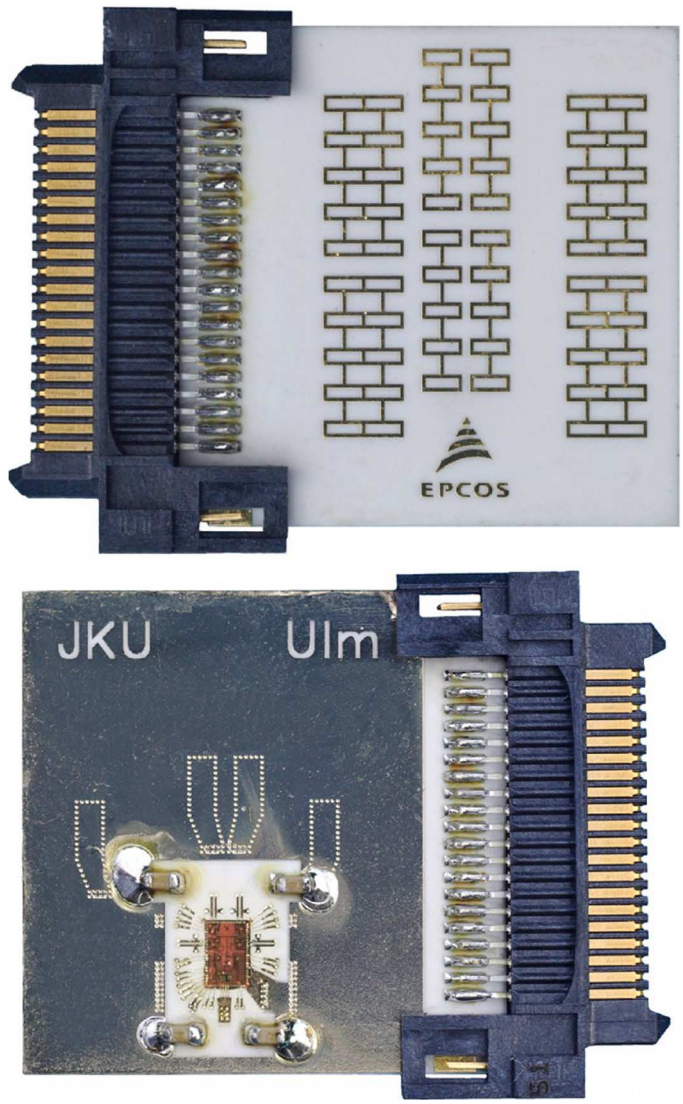


Fig. 1. Photograph of the front and rear sides of the frontend.

In this paper, we focus on the design of microstrip grid array antennas and use these to build a radar frontend in LTCC (see Fig. 1). The proposed antennas are operated in a traveling-wave mode with matched terminating elements. The traveling-wave excitation assures a wideband matching of the antenna and can be used to adjust an amplitude tapering. The inevitable beam tilt over frequency of a series-fed array can be encountered by using two sub-arrays with oppositely directed excitation.

In previous study [6], a 79-GHz radar frontend with patch antennas was designed and fabricated in LTCC technology. To

Manuscript received October 25, 2012; revised April 22, 2013; accepted April 23, 2013. Date of publication May 13, 2013; date of current version May 31, 2013. This work was supported by the Bundesministerium für Verkehr, Innovation und Technologie (BMVIT) and the Austrian Research Promotion Agency (FFG) within the co-funded Project InRaS in the strategic objective FIT-IT Systems on Chip.

F. Bauer and W. Menzel are with the Institute of Microwave Techniques, University of Ulm, D-89069 Ulm, Germany (e-mail: frank.bauer@uni-ulm.de; wolfgang.menzel@uni-ulm.de).

X. Wang and A. Stelzer are with the Institute for Communications Engineering and RF-Systems, Johannes Kepler University Linz, Linz A-4040, Austria (e-mail: x.wang@nthfs.jku.at; a.stelzer@nthfs.jku.at).

Color versions of one or more of the figures in this paper are available online at http://ieeexplore.ieee.org.

Digital Object Identifier 10.1109/TMTT.2013.2260766

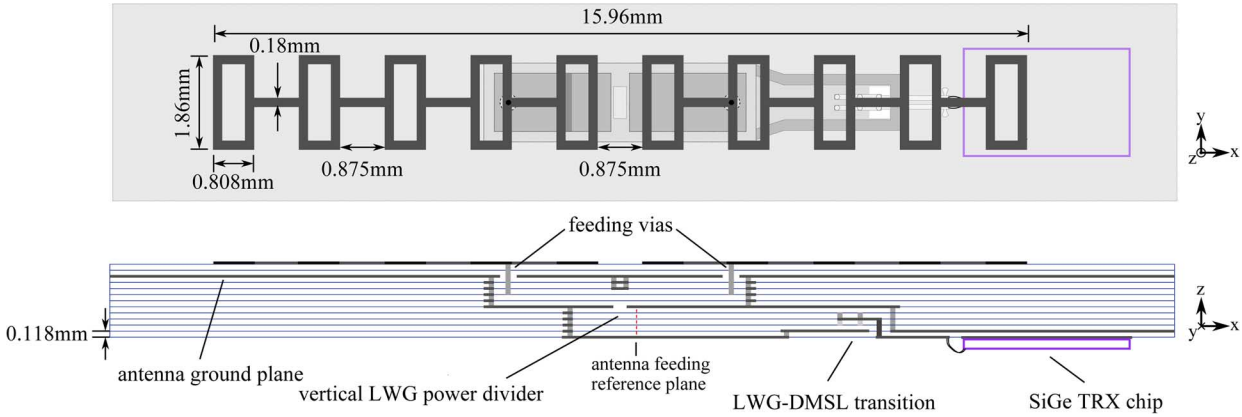


Fig. 2. SGA antenna with LWG feeding network.

overcome the fabrication tolerances caused by the shrinkage of the previously used benchmark (BM) LTCC system ($\epsilon_r = 7.4$, $\tan\delta = 0.002$) nonshrinkage loss optimized TDK LTCC [7] is used in this work. For high accuracy on the outer metallization layers, this material additionally offers the possibility of a high-precision fine-line photo-imaging process; however, its dielectric loss ($\epsilon_r = 7.3$, $\tan\delta = 0.0055$) is significantly higher compared to the BM material. Therefore, optimizations are necessary to improve the radar performance focused on antennas, wire-bond matching structure, and system configuration. To combine the advantages of both materials, a TDK high-frequency (HF) LTCC material ($\epsilon_r = 7.7$, $\tan\delta = 0.0025$) is currently under development and shall replace the used standard material in future designs.

A total of four grid antennas are used with an SiGe transceiver chip [5] offering four TRX channels. Using a laminated waveguide (LWG)-based feeding network, the antennas and transceiver chip can be placed on opposite sides, thus reducing spurious radiation and total dimensions of the sensor. Using multiple-input multiple-output (MIMO) techniques in the digital domain, the angular resolution can be improved.

This paper is organized as follows. First, a single grid array antenna and its feeding network is investigated. In Section III, a butterfly bond matching structure is described. Section IV discusses the system configuration and demonstrates first experimental results of the radar sensor.

## II. Grid Antenna With Feeding Network

A key component of the presented sensor is the microstrip grid array antenna. The concept was originally presented by Kraus in 1964 [8], and a first microstrip version was proposed by Conti *et al.* in 1981 [9]. Within the last years, the concept found its way into various fields of applications, such as 60-GHz radio [10] and 79-GHz automotive radar antennas [11], [12]. Grid array antennas can, in general, be subdivided into two main categories: resonant and traveling-wave implementations. Resonant grid array antennas have a perpendicular radiation, but usually have a narrow impedance bandwidth. An amplitude tapering is normally achieved by the line widths of the short sides of the antenna [9]. Traveling-wave grid antennas with a phase progression along the radiating elements as presented in [13] generate a tilted beam, but have a wide impedance bandwidth. Broadside beam operation of series-fed traveling-wave antennas is often avoided since a bad matching is obtained if element spacing equals a multiple of half wavelengths. Furthermore, traveling-wave antennas require a matched load at the end.

### A. Antenna Design

For multichannel radar applications with digital beamforming (DBF), a narrow beam of a single antenna is only desirable in the elevation plane, whereas the azimuth beamwidth defines the overall field of view.

The antenna array in this work is based on an LWG-fed traveling-wave grid antenna in which the necessary matched loads are provided by matched radiating end-elements. A complete single-row antenna including its corresponding feeding network is shown in Fig. 2. The antenna consists of two symmetric subarrays on two layers of TDK loss optimized standard LTCC (sintered layer thickness $t = 118\ \mu$m) both being fed by via probes reaching into an LWG. In a first design step, the antenna sub-arrays are considered separately from the feeding network and are assumed to be fed by a coaxial port from below. Since the via diameter is fixed at a value of $d_{\text{via}} = 0.1$ mm due to the LTCC manufacturing process, the impedance of the coaxial port is limited to a range of up to 27 $\Omega$ in order to keep the outer diameter of the coaxial port below a quarter-wavelength. The coaxial port feeds two microstrip lines (MSLs) in parallel whose impedances were therefore chosen to 54 $\Omega$ corresponding to a line width of 0.18 mm. The principal function of the antenna can be explained considering a fundamental element within a sub-array, as shown in Fig. 3(a). The rectangular loops have a length of $l = \lambda_{\text{MSL}}$ and a width $w = \lambda_{\text{MSL}}/2$ with $\lambda_{\text{MSL}}$ being the guided wavelength on the MSL. The arrows indicate the instantaneous currents in the loop. The currents flowing in the $x$-direction combine constructively, whereas the currents flowing in the $y$-direction have destructive interference. Hence, linear polarized radiation in the $x$-direction occurs. The cell width $w$ is set to a half-wavelength and the cell length $l$ is adjusted for a phase difference of 180° between A and A′ [see Fig. 3(a)]. For a broadside radiation, the phase difference between points B and B′ has to be 0°, which is controlled by the lengths $l_c$ of the connecting lines. Since the antenna is coaxially fed from below,

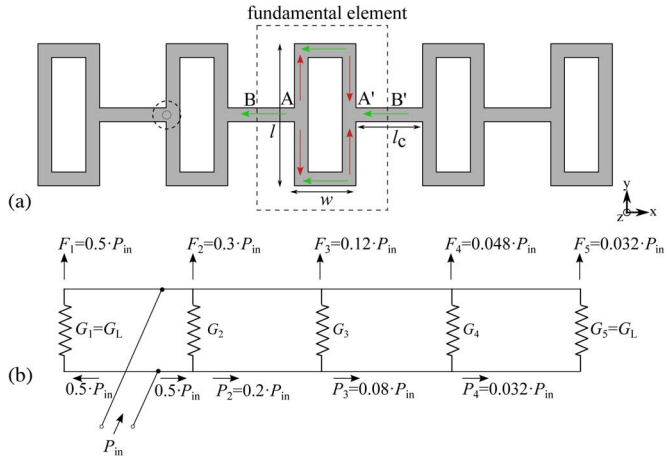


Fig. 3. Sub-array with chain and matched end-elements. (a) Current flow on fundamental element. (b) Simplified equivalent circuit representation.

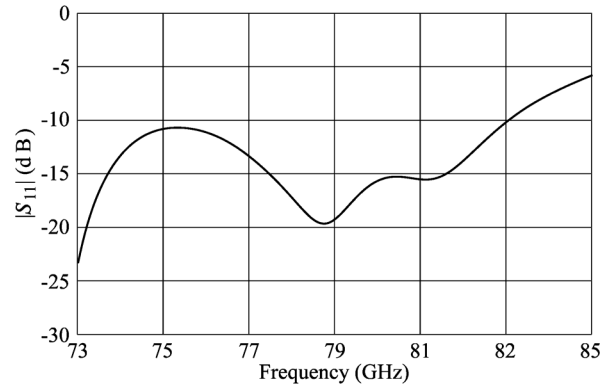


Fig. 4. Simulated reflection coefficient of coaxial fed sub-array.

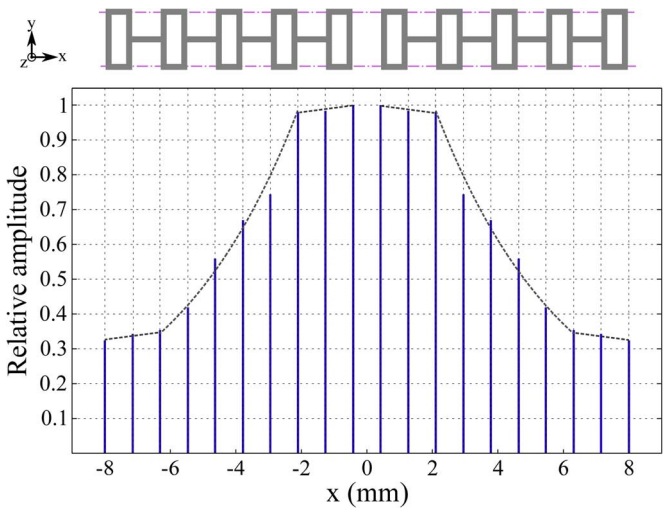


Fig. 5. Amplitude distribution on the SGA antenna at 79 GHz.

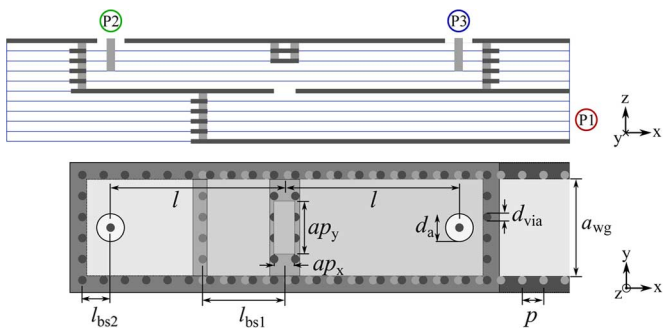


Fig. 6. Layer stack and top view of the LWG-power divider. Parameters: $l$ = 2.07 mm, $ap_x$ = 0.26 mm, $ap_y$ = 0.64 mm, $l_{\mathrm{bs1}}$ = 0.97 mm, $l_{\mathrm{bs2}}$ = 0.33 mm, $p$ = 0.25 mm, $d_a$ = 0.33 mm, $d_{\mathrm{via}}$ = 0.18 mm, and $a_{wg}$ = 1.15 mm.

each sub-array requires two matched loads realized by radiating elements. Fig. 3(b) shows a simplified equivalent-circuit representation of the sub-array. The input power $P_{\mathrm{in}}$ is split into two equal parts, one half being radiated by a matched element $G_{\mathrm{L}}$ on the left side. The other part passes the chain elements $(G_{1,\ldots,4})$ and is decreased by 60% per element due to radiation of the identical chain elements. The values $F_n$ in Fig. 3(b) show the radiated power per element with $P_n$ corresponding to the residual power after the $n$th element. The last matched element radiates the residual power of 3.2% of the input power. The amount of radiated power within each chain element is mainly dependent on the chosen substrate height, but also on the width of the MSL. In contrast to many weakly radiating elements, usually used in traveling-wave designs, strong radiation of each chain element is necessary in order to obtain a rapidly decreasing amplitude distribution along the array within the limited area of the sensor. Chain elements designed for strong radiation, however, cannot be perfectly matched at the same time. Hence, a full-wave analysis of the whole sub-array is indispensable. The simulated reflection coefficient of a sub-array is depicted in Fig. 4 and shows a wideband impedance matching. After mirror-symmetrical extension with a second sub-array, one obtains the amplitude distribution in elevation shown in Fig. 5. The amplitude distribution was obtained from the sampled $E$-field in the $x$-direction along the intersecting lines also shown in Fig. 5 and results in a simulated 3-dB beamwidth of 14.5° with −20-dB sidelobe level (SLL) in the $E$-plane and 58° in the $H$-plane. Mirroring the antenna along the $x$-axis and adjusting the feed position leads to a double-row grid array (DGA) antenna (see legend of Fig. 13). The double-row grid antenna has more gain, but also a reduced 3-dB beamwidth in the $H$-plane of 40°. Both antennas require a 180° phase shift and equal power at the feeding vias in order to obtain a symmetric phase and amplitude distribution. This can be achieved with an LWG feeding network below the antenna.

### *B. LWG Feeding Network*

The LWG power divider shown in Fig. 6 consists of two stacked LWGs using a total of ten layers. The lower LWG is terminated by a via-wall placed $l_{\mathrm{bs1}} \approx \lambda_{\mathrm{LWG}}/2$ away from the center of the coupling aperture, which provides an inherent phase shift of 180° for the two signals in the upper LWG. The local reduction of the upper LWG height above the aperture helps to improve the bandwidth of the transition. The simulated $S$-parameters (port numeration according to Fig. 6) given in Fig. 7 show a symmetric splitting with 180° phase shift and a return loss greater than 15 dB between 76–82 GHz. The feeding network completely realized below the antenna has the advantage that no restrictions with respect to antenna positions are present. Furthermore, the amount of spurious radiation due

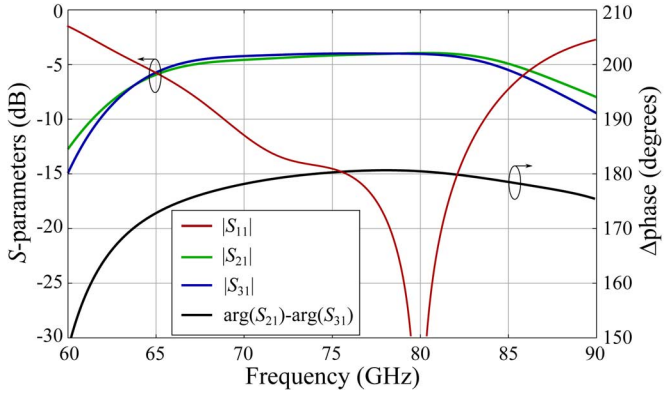


Fig. 7. Simulated $S$-parameters of the LWG power divider.

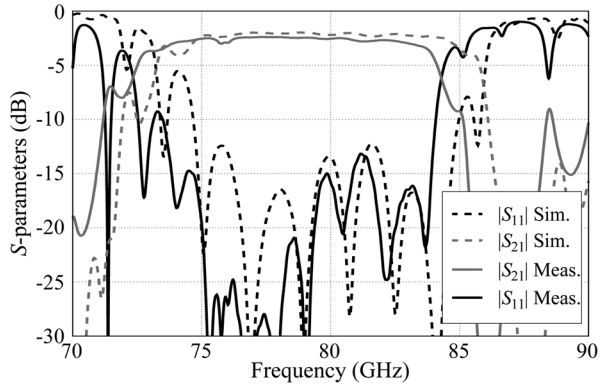


Fig. 9. $S$-parameters (back-to-back) of broadband WR-12 to LWG transition used for antenna characterization.

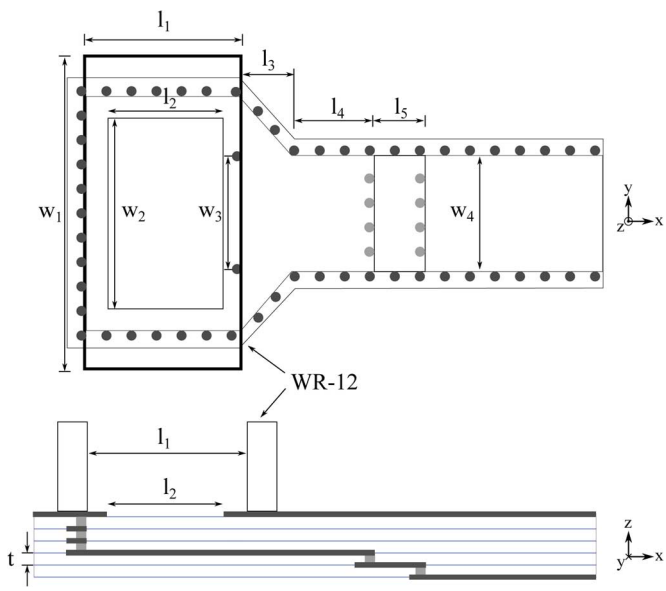


Fig. 8. Top and cross-section view of broadband WR-12 to LWG transition. Design parameters: $w_1 = 3.1$ mm, $w_2 = 1.89$ mm, $w_3 = 1.23$ mm, $w_4 = 1.15$ mm, $l_1 = 1.55$ mm, $l_2 = 1.14$ mm, $l_3 = 0.56$ mm, $l_4 = 0.8$ mm, $l_5 = 0.5$ mm, and $t = 0.118$ mm.

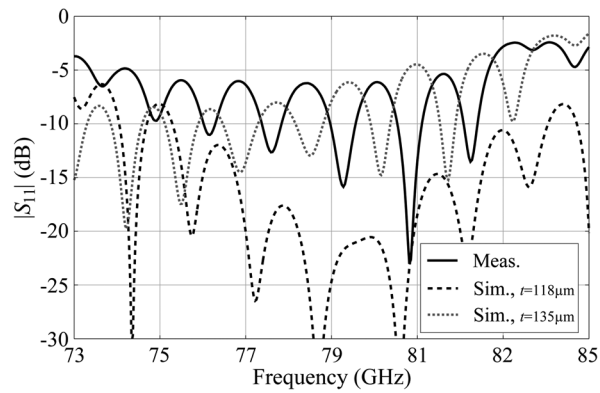


Fig. 10. Return loss of SGA antenna including measurement transition.

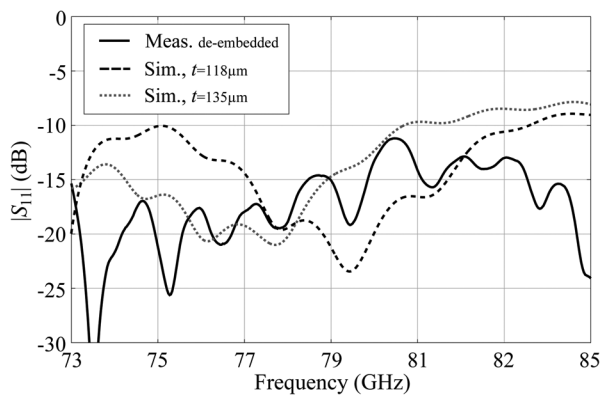


Fig. 11. Return loss of SGA antenna, de-embedded, time-gate 200 ps.

to the differential bond interconnects between the monolithic microwave integrated circuit (MMIC) and the differential microstrip lines (DMSLs) is reduced to a minimum with the TRX chip placed on the rear side of the LTCC frontend.

### C. Antenna Measurements

For antenna characterization, a wideband transition from WR-12 waveguide to LWG based on [14] has been designed (Fig. 8). An LTCC cavity comprising three layers with thickness of $t = 118$ $\mu$m is used to connect a vertically orientated air-filled waveguide to the LWG. The desired LWG height of five layers is achieved using a staircase structure. The transition dimensions are optimized for operation in the 76–81-GHz range. The measurement results of a back-to-back configuration are shown in Fig. 9. The transition has a bandwidth of more than 10 GHz with respect to 10-dB return loss.

The measurement of the antenna reflection coefficient including the measurement transition is shown in Fig. 10. The poor matching is caused by an increased LTCC layer thickness of $t = 135$ $\mu$m, which was observed after sintering of the antenna panel. The cavity depth of the transition comprising three LTCC layers is increased by 51 $\mu$m, which significantly degrades the performance of the transition. The performance of the antenna itself is hardly affected. In order to estimate the antenna matching without the influence of the transition, time gating with a width of 200 ps is applied to the measured $S$-parameters. Since the time gating is not applied to a structure with a sufficiently long homogeneous transmission line between transition and antenna, it should be clear that this method can only give a rough estimate of the antenna matching without the transition. However, comparing the de-embedded measurement with the simulated antenna reflection coefficient without transition at a layer thickness of $t = 135$ $\mu$m shows

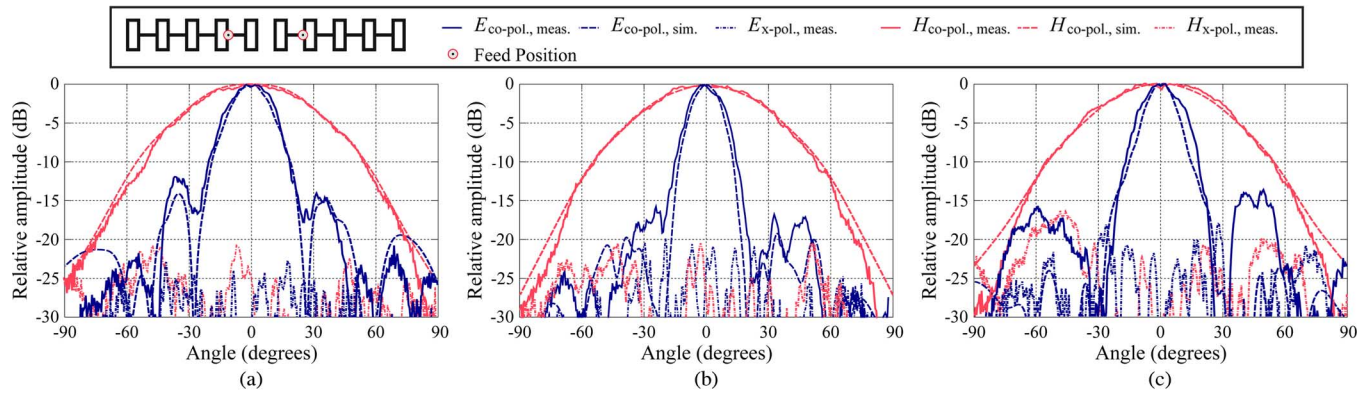


Fig. 12. Measured and simulated radiation diagrams of SGA antenna. (a) 77.5 GHz. (b) 79 GHz. (c) 80.5 GHz.

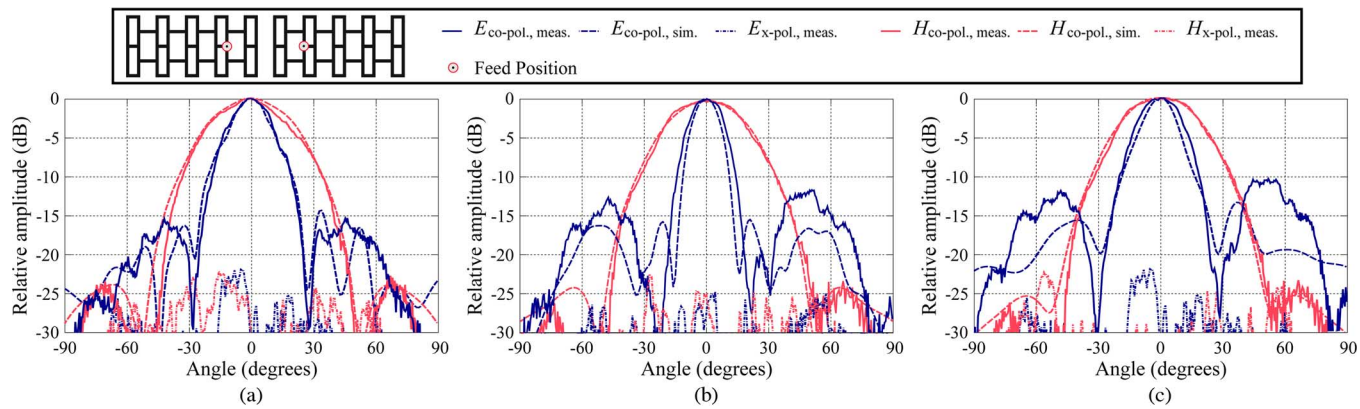


Fig. 13. Measured and simulated radiation diagrams of DGA antenna. (a) 77.5 GHz. (b) 79 GHz. (c) 80.5 GHz.

reasonable good agreement and reveals a slight frequency shift toward lower frequencies (Fig. 11). The reason for the increased layer thickness is still to be investigated.

The measured $E$- and $H$-plane radiation diagrams of a single-row grid array (SGA) antenna are plotted in Fig. 12. The 3-dB beamwidth at 79 GHz is 16° in elevation ($E$-plane) and 58° in azimuth ($H$-plane). The measured SLL in elevation amounts to approximately $-16$ dB. The results for a double row are shown in Fig. 13 with a 3-dB beamwidth of 16.5° in elevation and 40° in azimuth at 79 GHz. The calibrated measured gain taking into account the loss due to the feeding line and transition is 12.4 dBi for the single-row antenna and 14 dBi for the double-row grid antenna (reference plane for the gain, as depicted in Fig. 2). The simulated directivity of both antennas is 15.2 and 17.4 dBi, respectively. The reduced gain is partly caused by the bad matching of the transition, but the main reason is the still relatively high dielectric loss of the used TDK loss optimized standard LTCC material. For both antenna types, no considerable deterioration of the antenna pattern has been found in the frequency range from 77.5 to 80.5 GHz (SLL $< -10$ dB). Both antennas show a low measured cross-polarization level being more than 20 dB below the co-polarization level in the vicinity of boresight direction and more than 15 dB within an angular range of $\pm 40°$ in the azimuth plane.

## III. Wire-Bond Matching Structure

Besides the LWG-to-DMSL transition presented in [15], bond wires are necessary to finally connect the antennas to the MMIC. In [6], a high–low-impedance-line concept was used. However, this has two essential drawbacks, which are: 1) two stages of quarter-wavelength transformers increase the total length of the matching structure and 2) this structure requires careful die placement and is susceptible to die misalignment. To this end, a so-called butterfly matching structure was developed. The idea of this bond matching structure shown in Fig. 14 is to use the inductive behavior of short-circuited stubs to cancel the inductance of the bond wires. At the given stub lengths, the short-circuited stubs show inductive behavior. Using a quarter-wavelength transmission line, the inductance of the stubs is converted to a capacitance, and hence, the bond wire inductance is canceled. To verify the assumption, two 100-Ω DMSL (100-$\mu$m line/space) in the back-to-back configuration connected with a differential gold bond (25-$\mu$m diameter, and 200-$\mu$m height above the substrate) were simulated; the distance between the two bond footprints is 200 $\mu$m. The simulation results with and without a butterfly matching structure are shown in Fig. 15. It can be seen that the matching structure significantly improves the reflection/transmission performance in the operating frequency band.

After wire bonding, the reflection factor of the butterfly matching structure with the MMIC [5] was measured and transferred to mixed mode $S$-parameters [16]. The test fixture for the measurement is identical to that in [6]. Fig. 16 shows the measured differential reflection factor $S_{11dd}$.

The measurement of the insertion loss of the bond wire with the matching structure is difficult since no test chip as in [17] for a back-to-back measurement is available. Alternatively, the

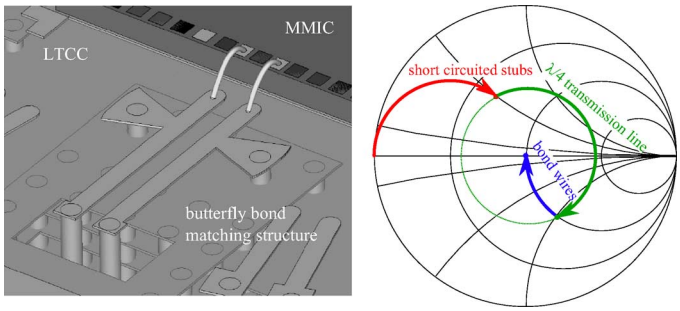


Fig. 14. 3-D model of the butterfly bond matching structure and functionality by means of Smith chart.

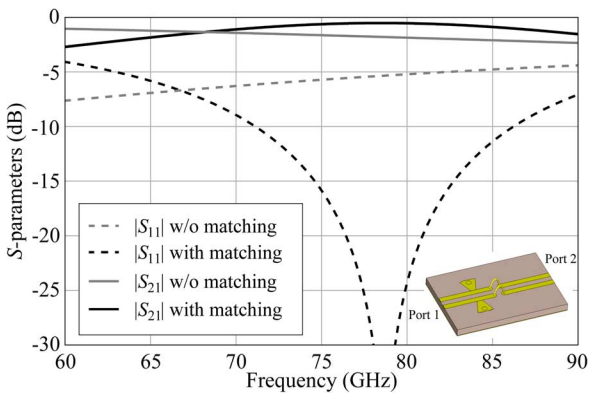


Fig. 15. Simulated $S$-parameters of differential bond wire with and without butterfly bond matching structure.

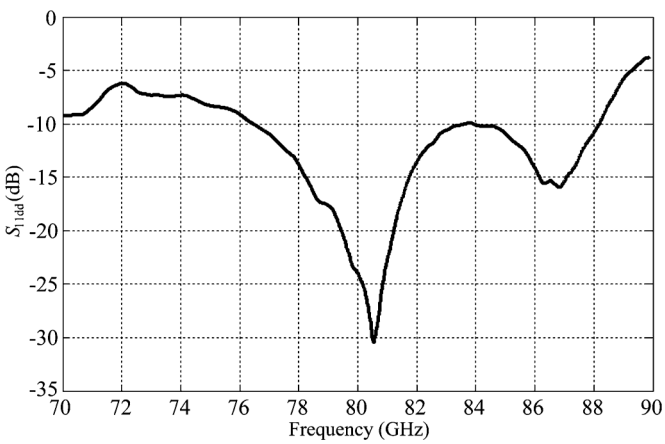


Fig. 16. Measured differential reflection factor of the butterfly matching structure with the MMIC bonded.

MMIC was activated, the power on the MSL (including the losses of the bond wires, the matching structure, and a balun) was measured. After calculation, the insertion loss of the bond-wire interconnects with the matching structure varies between 0.7–1.5 dB in the whole operating frequency band of the chip.

## IV. 79-GHz LTCC Radar Sensor

With the components presented in the previous sections, a short-range radar sensor is built using a four-channel fully differential transceiver chip in SiGe technology [5], the characteristics of which are summarized in Table I. The block diagram of the sensor based on the frequency modulated continuous wave (FMCW) principle is shown in Fig. 17: The on-chip voltage-controlled oscillator (VCO) generates a signal in the frequency band from 77 to 81 GHz. A part of the VCO signal

TABLE I
Summary of Transceiver Chip MMIC Characteristics

| Number | Position (mm) |
|---|---|
| Supply Voltage | 3.3 V |
| Supply Current | 1218 mA |
| Temperature Range | -40 °C – 125 °C |
| Tuning Range | 77 GHz – 81 GHz |
| Phase Noise (dBc/Hz@100kHz) | -75 |
| Conversion Gain | 10 dB |
| Noise Figure | 16 dB |
| Output Power (bond pads) | 6 dBm (@25 °C) |

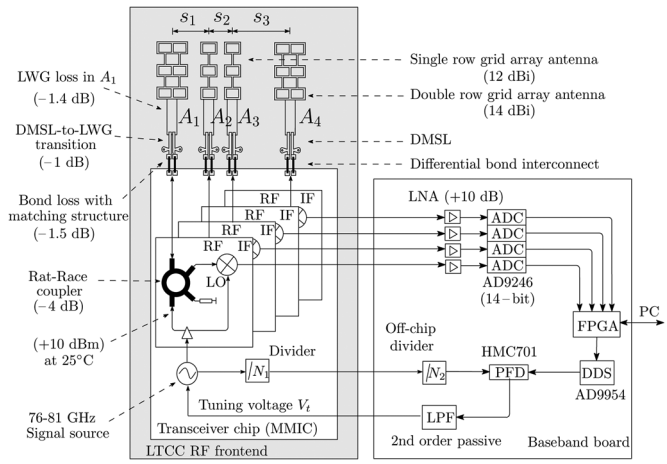


Fig. 17. Block diagram of the LTCC radar sensor.

is fed to the LO port of the mixer, the received signal from the target arrives at the RF port. The frequency difference between the transmitted and received signal is then directly generated at the IF port. The IF signals of each channel are amplified and converted to digital signals by the analog-to-digital converters (ADCs). With an on-chip divider (with configurable divider factor $N_1$), the VCO signal is down-scaled and connected to an off-chip phase-locked loop for frequency ramp generation. The total divider factor of the VCO signal is 1024 (on-chip divider factor $N_1 = 32$ and off-chip divider factor of $N_2 = 32$). A phase frequency detector (PFD) compares the divided VCO signal (around 76 MHz) with the reference signal generated by a direct digital synthesizer (DDS). A second-order passive loop filter (LPF) converts the charge-pump output current of the PFD to the tuning voltage $V_t$. All these components are controlled by a field programmable gate array (FPGA).

For the cross-range imaging, DBF is applied. The size of the LTCC RF-frontend is 23 mm × 23 mm. After excluding the area for the second-level interconnects and the edge margins (see Fig. 1), the usable area for the antenna is around 13 mm × 20 mm. The 3-dB beamwidth of the grid array antenna in the vertical elevation plane is determined by its physical length and has been presented in Section II. In the azimuth, i.e., scanning plane, the angular resolution can be improved by using a MIMO concept combining a nonuniformly spaced array [18].

As stated above, the MMIC provides four channels (denoted as $A_{1,\ldots,4}$ from left to right). Each channel is capable to transmit (Tx) and receive (Rx) signals simultaneously. Applying the MIMO concept, each Tx path is switched on (from $A_{1,\ldots,4}$), while the Rx paths of all channels are kept active. By choosing suitable antenna spacings $S_1/S_2/S_3 = 3.6/2.2/5.4$ mm and

TABLE II
POSITIONS AND TYPE OF THE VIRTUAL ANTENNAS

| Number | Position (mm) | Type |
|---|---|---|
| 1 | 0 (phase center) | 3 (DGA for TRx) |
| 2 | 3.6 | 2 (DGA for Tx or Rx) |
| 3 | 5.8 | 2 |
| 4 | 7.2 | 1 (SGA for TRx) |
| 5 | 9.4 | 1 |
| 6 | 11.2 | 3 |
| 7 | 11.6 | 1 |
| 8 | 14.8 | 2 |
| 9 | 17 | 2 |
| 10 | 22.4 | 3 |

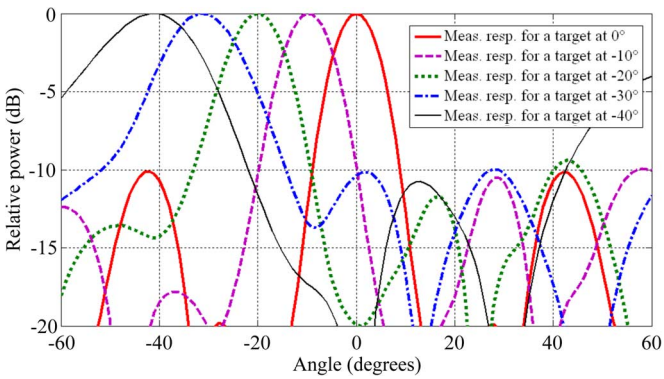


Fig. 18. Measured responses of the radar sensor to a target at $-40°$, $-30°$, $-20°$, $-10°$, and $0°$.

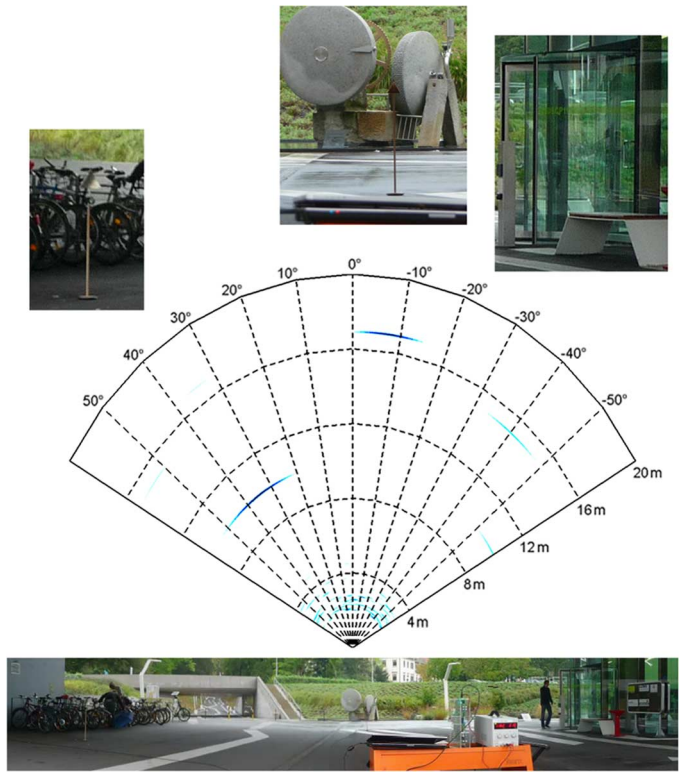


Fig. 19. Field measurement results of the LTCC radar sensor.

weightings, which were obtained using convex optimization [19], ten virtual antennas with different positions are synthesized. Thereby, the virtual antenna aperture can be enlarged to twice the physical size. Using a nonuniform array, the ambiguity problem in the array factor can be mitigated. As array elements both SGA antennas and DGA antennas (see Fig. 17) are employed. DGAs and SGAs are used for channels $A_{1,4}$ and $A_{2,3}$, respectively. Since the DGA has approximately 2 dB more gain than the SGA, the detecting range in the direction of interest can be improved, however, at the cost of field of view.

Introducing nonidentical array elements, the synthesized ten virtual antennas are now categorized into three types. Type 1: SGA used for both Tx and Rx. Type 2: DGA used for Tx and SGA for Rx (or vice versa). Type 3: DGA used for both Tx and Rx. The relative virtual antenna positions and the types of the virtual antennas are listed in Table II. Normalized to the received signals of the type 1 virtual antenna, the magnitudes of the received signals of the type 2 and 3 virtual antennas are angle dependent, rising the SLL at different angles for the target response during the DBF process. However, the sidelobe can be suppressed by using optimized weighting factors. Details about the choice of the antenna spacings and the optimization methods are outside the focus of this paper. The fabricated LTCC radar frontend using a total of 12 ceramic layers is shown in Fig. 1.

## V. MEASUREMENT RESULTS

At 79 GHz, the measured effective isotropic radiated power of channel $A_1$ (DGA antenna, 14-dBi gain) is 13.1 dBm. Using the on-chip temperature sensor, the measured operating temperature of the radar sensor is 94°. Assuming the output power of the power amplifier is reduced from 10 dBm (at 25°) to 7 dBm at 94°, the total passive power loss within the radar amounts to approximately 8 dB (see Fig. 17). Using TDK HF material in future designs, this loss could be reduced by 2.7 dB (0.7-dB LWG feed network, 2-dB more antenna gain). The noise figure of the radar RF frontend is around 20 dB, which is mainly determined by the loss of the passive elements (8 dB) and the noise figure of the mixer of the MMIC (12 dB). For the distance measurement, the frequency is swept from 77.5 to 80.5 GHz within 1 ms. The minimal angular resolution in the azimuth plane is $\leq 9°$. The angular measurements were conducted in an anechoic chamber. As targets corner reflectors were used. The measured responses of the radar sensor to a target at different angles are shown in Fig. 18. The realized field of view of the radar is 80°. The measurement results of an arrangement of three reflectors are shown in Fig. 19. The center corner reflector has a radar cross section of 11 dB square meters (dBsm) at 79 GHz.

## VI. CONCLUSION

In this paper, 79-GHz microstrip grid array antennas applied to a 79-GHz FMCW radar sensor in LTCC technology have been presented. Using an LWG feeding network, a very compact and highly integrated sensor design could be achieved. Despite the encountered manufacturing problems concerning the layer thickness, the presented antennas on LTCC show a wide impedance bandwidth and an adequate radiation performance. With the future availability of improved low-loss LTCC material systems, the presented sensor concept offers a promising solution for automotive radar applications in the 79-GHz SRR band.

## ACKNOWLEDGMENT

The authors would like to thank M. Stadler, K. Aichholzer, S. Brunner, B. Hampel, and F. Rak, all with EPCOS OHG, Deutschlandsberg, Austria, for fabricating the ceramic panel.

## REFERENCES

[1] W. Menzel, "Millimeter-wave radar for civil applications," in *Eur. Radar Conf.*, Oct. 2010, pp. 89–92.
[2] K. Strohm, H.-L. Bloecher, R. Schneider, and J. Wenger, "Development of future short range radar technology," in *Eur. Radar Conf.*, Oct. 2005, pp. 165–168.
[3] J. Hasch, E. Topak, R. Schnabel, T. Zwick, R. Weigel, and C. Waldschmidt, "Millimeter-wave technology for automotive radar sensors in the 77 GHz frequency band," *IEEE Trans. Microw. Theory Techn.*, vol. 60, no. 3, pp. 845–860, Mar. 2012.
[4] S. Pacheco, R. Reuter, S. Trotta, D. Salle, and J. John, "SiGe technology and circuits for automotive radar applications," in *11th IEEE Silicon Monolithic Integr. Circuits in RF Syst. Top. Meeting*, Jan. 2011, pp. 141–144.
[5] H. Forstner, H. Knapp, H. Jager, E. Kolmhofer, J. Platz, F. Starzer, M. Treml, A. Schinko, G. Birschkus, J. Bock, K. Aufinger, R. Lachner, T. Meister, H. Schafer, D. Lukashevich, S. Boguth, A. Fischer, F. Reininger, L. Maurer, J. Minichshofer, and D. Steinbuch, "A 77 GHz 4-channel automotive radar transceiver in SiGe," in *IEEE Radio Freq. Integr. Circuits Symp.*, Apr. 2008, pp. 233–236.
[6] X. Wang and A. Stelzer, "A 79-GHz LTCC RF-frontend for short-range applications," in *IEEE MTT-S Int. Microw. Symp. Dig.*, Jun. 2011, pp. 1–4.
[7] S. Brunner, M. Stadler, X. Wang, F. Bauer, and K. Aichholzer, "Advanced high frequency LTCC technology for applications beyond 60 GHz," in *Proc. 8th Int. Ceram. Interconnect and Ceram. Microsyst. Technol. Conf.*, Erfurt, Germany, Apr. 2012, pp. 77–81.
[8] J. Kraus, "A backward angle-fire array antenna," *IEEE Trans. Antennas Propag.*, vol. AP-12, no. 1, pp. 48–50, Jan. 1964.
[9] R. Conti, J. Toth, T. Dowling, and J. Weiss, "The wire grid microstrip antenna," *IEEE Trans. Antennas Propag.*, vol. AP-29, no. 1, pp. 157–166, Jan. 1981.
[10] B. Zhang and Y. P. Zhang, "Grid array antennas with subarrays and multiple feeds for 60-GHz radios," *IEEE Trans. Antennas Propag.*, vol. 60, no. 5, pp. 2270–2275, May 2012.
[11] M. Frei, F. Bauer, W. Menzel, A. Stelzer, and L. Maurer, "A 79 GHz differentially fed grid array antenna," in *Eur. Radar Conf.*, Oct. 2011, pp. 432–435.
[12] F. Bauer and W. Menzel, "A 79 GHz microstrip grid array antenna using a laminated waveguide feed in LTCC," in *IEEE Int. Antennas Propag. Symp.*, Jul. 2011, pp. 2067–2070.
[13] M. Tiuri, S. Tallqvist, and S. Urpo, "Chain antenna," in *IEEE Int. Antennas Propag. Soc. Symp.*, Jun. 1974, vol. 12, pp. 274–277.
[14] W. Byun, B.-S. Kim, K.-S. Kim, K.-C. Eun, M. S. Song, R. Kulke, O. Kersten, G. Mollenbeck, and M. Rittweger, "Design of vertical transition for 40 GHz transceiver module using LTCC technology," in *Eur. Microw. Conf.*, Oct. 2007, pp. 1353–1356.
[15] X. Wang and A. Stelzer, "A 79-GHz LTCC differential microstrip line to laminated waveguide transition using high permittivity material," in *Proc. Asia–Pacific Microw. Conf.*, Dec. 2010, pp. 1593–1596.
[16] D. Bockelman and W. Eisenstadt, "Combined differential and common-mode scattering parameters: Theory and simulation," *IEEE Trans. Microw. Theory Techn.*, vol. 43, no. 7, pp. 1530–1539, Jul. 1995.
[17] G. Liu, A. Trasser, A. Ulusoy, and H. Schumacher, "Low-loss, low-cost, IC-to-board bondwire interconnects for millimeter-wave applications," in *IEEE MTT-S Int. Microw. Symp. Dig.*, Jun. 2011, pp. 1–4.
[18] R. Feger, C. Wagner, S. Schuster, S. Scheiblhofer, H. Jager, and A. Stelzer, "A 77-GHz FMCW MIMO radar based on an SiGe single-chip transceiver," *IEEE Trans. Microw. Theory Techn.*, vol. 57, no. 5, pp. 1020–1035, May 2009.
[19] H. Lebret and S. Boyd, "Antenna array pattern synthesis via convex optimization," *IEEE Trans. Signal Process.*, vol. 45, no. 3, pp. 526–532, 1997.

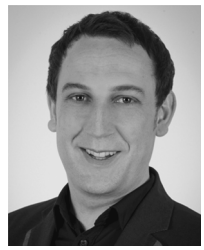

**Frank Bauer** (S'10) received the Dipl.-Ing. degree in electrical engineering from the University of Ulm, Ulm, Germany, in 2009.

Since 2009, he has been with the Institute of Microwave Techniques, University of Ulm. His main research topics are millimeter-wave antennas and components.

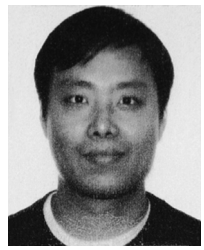

**Xin Wang** received the Dipl.-Ing. degree in electrical engineering from Friedrich-Alexander-University Erlangen–Nuremberg, Germany, in 2009.

Since 2009, he has been with the Institute for Communications Engineering and RF-Systems, Johannes Kepler University Linz, Linz, Austria, as a Research Assistant. His research interest is microwave applications.

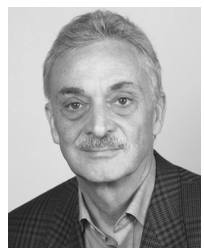

**Wolfgang Menzel** (M'89–SM'90–F'01) received the Dipl.-Ing. degree in electrical engineering from the Technical University of Aachen, Aachen, Germany, in 1974, and the Dr.-Ing. degree from the University of Duisburg, Duisburg, Germany, in 1977.

From 1979 to 1989, he was with the Millimeter-Wave Department, AEG [now the European Aerospace, Defense, and Space Systems (EADS)], Ulm, Germany . In 1989, he became a Full Professor with the Institute of Microwave Techniques, University of Ulm, Ulm, Germany. His current areas of interest are multilayer planar circuits, waveguide filters and components, antennas, interconnects and packaging, and millimeter-wave application and system aspects.

Dr. Menzel was an associate editor for the IEEE TRANSACTIONS ON MICROWAVE THEORY AND TECHNIQUES (2003–2005). From 1997 to 1999, he was a Distinguished Microwave Lecturer for Microwave/Millimeter Wave Packaging. From 1997 to 2001, he chaired the German IEEE Microwave Theory and Techniques (MTT)/Antennas and Propagation (AP) Chapter. He was the recipient of the 2002 European Microwave Prize.

**Andreas Stelzer** (M'00) was born in Haslach an der Mühl, Austria, in 1968. He received the Diploma Engineer degree in electrical engineering from the Technical University of Vienna, Vienna, Austria, in 1994, and the Dr.techn. degree (Ph.D.) in mechatronics (with sub auspiciis praesidentis rei publicae honors) from the Johannes Kepler University Linz, Linz, Austria, in 2000.

In 2003, he became an Associate Professor with the Institute for Communications and Information Engineering and RF Systems, Johannes Kepler University Linz. Since 2003, he has been a key Researcher for the Linz Center of Competence in Mechatronics (LCM). He is currently also a Researcher for the 2008 founded Austrian Center of Competence in Mechatronics (ACCM), where he is responsible for numerous industrial projects. Since 2007, he has been Head of the Christian Doppler Laboratory for Integrated Radar Sensors, and since 2011 a Full Professor with the Johannes Kepler University Linz, where he heads the Department for RF-Systems. He has authored or coauthored over 300 journal and conference papers. He is a reviewer for international journals and conferences. His research is focused on microwave sensor systems for industrial and automotive applications, RF and microwave subsystems, surface acoustic wave (SAW) sensor systems and applications, as well as digital signal processing for sensor signal evaluation.

Dr. Stelzer is a member of the Austrian ÖVE. He has served as an associate editor for the IEEE MICROWAVE AND WIRELESS COMPONENTS LETTERS. He was the recipient of several awards including the EEEfCOM Innovation Award and the European Microwave Association (EuMA) Radar Prize of the European Radar Conference. He was also the recipient of the 2011 German Microwave Conference (GeMiC) Best Paper Award, as well as the 2008 IEEE Microwave Theory and Techniques Society (IEEE MTT-S) Outstanding Young Engineer Award and the 2011 IEEE Microwave Prize.